Materials & Design 213 (2022) 110270

Contents lists available at ScienceDirect

Materials & Design

journal homepage: www.elsevier.com/locate/matdes

Steel-copper functionally graded material produced by twin-wire and arc additive manufacturing (T-WAAM)

Tiago A. Rodrigues [a,*], N. Bairrão [a], Francisco Werley Cipriano Farias [a], A. Shamsolhodaei [b], Jiajia Shen [a], N. Zhou [b], Emad Maawad [c], Norbert Schell [c], Telmo G. Santos [a], J.P. Oliveira [a,*]

[a] UNIDEMI, Department of Mechanical and Industrial Engineering, NOVA School of Science and Technology, Universidade NOVA de Lisboa, 2829-516 Caparica, Portugal
[b] Department of Mechanical and Mechatronics Engineering, University of Waterloo, Canada
[c] Helmholtz-Zentrum Hereon, Institute of Materials Physics, Max-Planck-Str. 1, Geesthacht 21502, Germany

HIGHLIGHTS

- Defect-free functionally graded material of HSLA steel to Cu-based alloy was successfully produced.
- By synchrotron X-ray diffraction the interface revealed a mixture of Cu (FCC), Fe (BCC), and Fe(FCC) in the interface region.
- Microhardness ranged from 260 HV_1 to 120 HV_1.

GRAPHICAL ABSTRACT

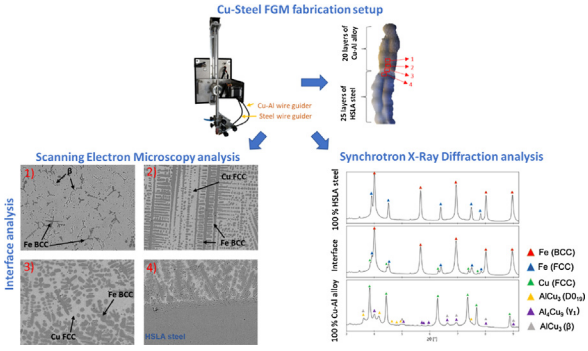

ARTICLE INFO

Article history:
Received 26 September 2021
Revised 17 November 2021
Accepted 21 November 2021
Available online 23 November 2021

Keywords:
Wire and arc additive manufacturing
Functionally Graded Material (FGM)
Copper alloy
High strength low alloy steel
Miscibility gap

ABSTRACT

In this work, a functionally graded material (FGM) part was fabricated by depositing a Cu-based alloy on top of a high strength low alloy (HSLA) steel by twin-wire and arc additive manufacturing (T-WAAM). Copper and steel parts are of interest in many industries since they can combine high thermal/electrical conductivity, wear resistance with excellent mechanical properties. However, mixing copper with steel is difficult due to mismatches in the coefficient of thermal expansion, in the melting temperature, and crystal structure. Moreover, the existence of a miscibility gap during solidification, when the melt is undercooled, causes serious phase separation and segregation during solidification which greatly affects the mechanical properties. Copper and steel control samples and the functionally graded material specimen were fabricated and investigated using optical microscopy, scanning electron microscopy, and high energy synchrotron X-ray diffraction. Retained δ-ferrite was found in a Cu matrix at the interface region due to regions with mixed composition. A smooth gradient of hardness and electric conductivity along the FGM sample height was obtained. An ultimate tensile strength of 690 MPa and an elongation at fracture of 16.6% were measured in the FGM part.

1. Introduction

The use of multiple wires simultaneously fed into the molten pool allows the fabrication of functionally graded materials (FGM) via Twin-wire and arc additive manufacturing (T-WAAM).

* Corresponding authors.
E-mail addresses: tma.rodrigues@campus.fct.unl.pt (T.A. Rodrigues), jp.oliveira@fct.unl.pt (J.P. Oliveira).

https://doi.org/10.1016/j.matdes.2021.110270
0264-1275/

Therefore, parts can have distinct properties (thermal/electric conductivity, corrosion resistance, hardness, ductility, for example) at different locations [1]. FGM can be composed either by gradual or abrupt transitions. Depending on the material combination selection, a direct interface (i.e., an abrupt transition) can experience large stresses and chemical incompatibility, while a continuous and gradual transition could minimize these issues. However, mixing multiple materials within the same melt pool can cause the formation of undesirable intermetallics compounds, which can reduce the weldability and processability (e.g., hot cracks and high hardness regions) and induce premature failure [2].

Among the combination of the metals that can be fabricated via T-WAAM, copper to steel multi-metallic parts have a major interest in the power generation industry, heat transfer components, electric conductors, cryogenic sector, and dies-casting industries [3]. If used in dies, the higher thermal conductivity of copper allows an intense heat extraction from the castings, which reduces the production times, manufacturing costs, and refine the microstructure by promoting faster cooling rates. Moreover, copper and its alloys often offer good wear and corrosion resistance, whereas steel provides excellent toughness and fatigue resistance.

Despite the above advantages and large application fields for copper-steel FGM, joining these materials is a difficult task. The mismatch in the thermal expansion coefficient (10 vs 17 $\times$ 10^{-6}/°C), originates large misfit strains and high residual stresses, which can lead to cracking. Also, the difference in the crystal structure and the low solubility of Cu in Fe are the origins of a lack of solid solution phases in the Fe—Cu phase diagram at low temperatures. In addition, the liquid Cu can penetrate the steel grain boundaries causing hot cracking (liquid metal embrittlement phenomena) [4]. Moreover, the Fe—Cu system exhibits a miscibility gap in which a metastable liquid-phase separation occurs by undercooling the melt pool. The occurrence of this liquid-phase separation greatly weakens the microstructure and may negatively influence the mechanical properties at the interface of the two materials [5].

Attempts to obtain components based on steel and copper-based alloys have been primarily tried via fusion-based welding [4,6,7]. However, weldability issues (hot cracks and brittle constituents) required the development of welding strategies capable of obtaining sound and high-performing structures. For example, a nickel interlayer has been proposed as a solution to make this dissimilar joint [8]. Later, this solution was employed during powder-based additive manufacturing, in which a Ni-based powder was used to create an interlayer between an H13 steel substrate and the top Cu layers. Without the interlayer of Ni, the abrupt transition from Cu to steel resulted in micro-cracks at the interfacial area. The authors attributed this to the combined effect of solidification cracking and high residual stresses, which were caused by the mismatch in the coefficients of thermal expansion and by consecutive cycles of expansion and shrinkage during subsequent layer depositions [9]. Another solution to successfully join these materials is the use of a pulsed welding heat source (e.g., electric arc or focused laser beam), which will avoid a deeper penetration of Cu onto the steel, i.e., low dilution [4].

Nevertheless, Cu to steel FGM has already been obtained with different additive manufacturing technologies. For example, with Laser Engineered Net Shaping™ (LENS) [10] a crack-free smooth transition was possible but with several pores observed. Similarly, a controlled gradient was possible with electron beam freeform fabrication (EBF^3) [11]. The authors determined that after three layers were deposited on top of a steel layer, no iron constituents could be found. X-ray diffraction results showed the presence of the metastable $FeCu_4$ in the first deposited copper layers, as a result of the slow cooling rates of EBF^3. When it comes to arc-based additive manufacturing structural components based on these materials have not been reported yet, to the best of the authors' knowledge.

Considering the above-mentioned issues, this study aimed to investigate and create an FGM composed of a Cu-based alloy and a high strength low alloy (HSLA) steel fabricated by T-WAAM. The microstructure and mechanical properties were investigated using correlative characterization techniques encompassing optical and electron microscopy, high-energy synchrotron X-ray diffraction, and mechanical property analysis.

2. Materials and methods

2.1. Experimental setup

In this work, T-WAAM parts were made using a welding machine *Spitfire TIG DC 1700 HF,* and an in-house developed multiple wire feed system adapted in a 3-axis customized table. Two different wires were used to fabricate the multi-material metallic part: ERCuAl-A2 (Cu—Al alloy) and ER-120S-G (HSLA steel). The chemical composition of the welding wires is presented in Table 1. A mild steel plate was used as the substrate with the size of 180 $\times$ 50 $\times$ 6 mm. The experimental setup is presented in Fig. 1. In addition, control samples (Cu—Al alloy and HSLA steel) were also fabricated.

Preliminary parameter selection enabled to obtain process parameters that resulted in a similar height and width for both materials and were chosen to fabricate three different samples: (i) 40 layers of high strength low alloy (HSLA) steel; (ii) 40 layers of Cu—Al alloy; (iii) 25 layers of HSLA-steel covered by 20 layers of Cu—Al alloy (Fig. 2). The fabricated parts were single walls with a lenght of 120 mm. The process parameters used are detailed in Table 2, notice that the current was set at 100 A for the steel layers and increased to 120 A in the Cu—Al layers. The need to increase the welding current to deposit the copper-based wire is related to its high thermal conductivity, which tends to rapidly dissipate the heat and creates a small molten pool.

2.2. Microstructural characterization

Cross-sections were cut, polished, and then etched. The steel microstructure was revealed using Nital (4%) reagent, and the main phases in the Cu—Al alloy were exposed with a solution of ethanol (71 ml), HCL (24 ml), and $FeCl_3$ (5 g). To identify the phases in the produced parts, high-energy synchrotron X-ray diffraction (SXRD) was performed at PETRA III, DESY (Hamburg, Germany). A beam energy of 87 kV (λ = 0.14235 A) was used. SXRD measurements were made with a beam size of 1 $\times$ 1 mm in intervals of 1 mm, covering the height of the FGM part. A *Leica DMI 5000 M* optical microscope and a Zeiss FESEM 1530 scanning electron microscope (SEM) equipped with an Energy Dispersive X-Ray Spectroscopy (EDS) system were used in this investigation. The Electron Backscatter Diffraction (EBSD) measurements were made using a JSM-7000F SEM. The nomenclature used for phase identification in the Cu—Al alloy was taken from the work of Wang et al. [12].

2.3. Mechanical testing

Microhardness testing was performed along the height of the sample with an indentation distance of 250 μm, a load of 4.9 N, and a dwell time of 10 s, using a *Mitutoyo HM-112* Hardness Testing Machine. Tensile tests were performed on a *Shimadzu autograph* equipped with an *AG 50 kN* load cell. The displacement rate was set at 1 mm/min and three tensile specimens for each condition (base materials and FGM) were tested to evaluate the reproducibility in terms of mechanical properties. Only vertical

Table 1
Chemical composition of the welding wires used (wt.%).

Alloy (AWS classification)	C	Mn	Si	Ni	Cr	Mo	Cu	Al	Fe
Copper-Aluminum (ERCuAl-A2)	–	0.5	–	0.5	–	–	89.7	8.5	0.8
HSLA steel (ER-120S-G)	0.1	1.8	0.7	1.9	0.3	0.5	–	–	94.7

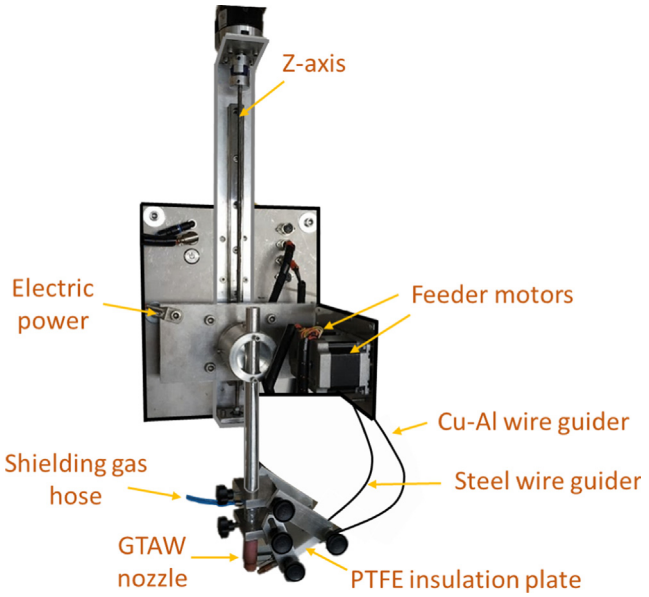

Fig. 1. Experimental setup of the multiple wire feeder based on a gas tungsten arc welding torch equipped in a customized 3-axis table.

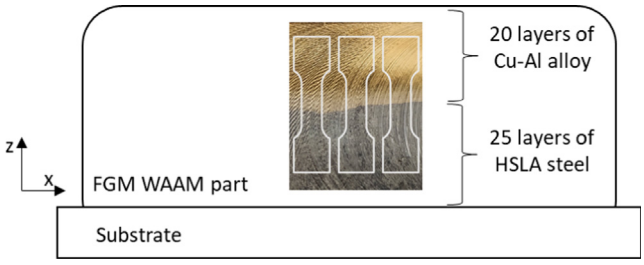

Fig. 2. Schematic representation of the functionality graded material of HSLA-steel to Cu-based alloy.

Table 2
Process parameters used in the experiments.

Process	Gas tungsten arc welding (GTAW)
Travel speed	100 mm/min
Wire feed speed	1 m/min
Current	100 A for HSLA steel layers; 120 A for Cu-based alloy layers
Shielding gas	Argon 99.99%
Shielding gas flow rate	18 L/min

specimens (aligned with the z-axis direction) were tested. The uniaxial tensile samples were machined to dimensions of 40 × 6 × 2 mm.

2.4. Electrical conductivity and magnetic permeability characterization

Magnetic permeability measurements were performed using an absolute helicoidally shielded eddy current (EC) probe with a 3 mm diameter from Olympus, operating in bridge mode. Calibration tests were made accordingly to previous work by Santos et al. [13]. To measure the changes in the FGM electrical conductivity, a four-point potential drop technique previously described in Sorger et al. [14] was used. Scan measurements started in the first steel layer and finished on the last deposited Copper layer. The probe has a needle spacing of 635 μm, and a current of 80 mA was imposed between the external needles.

3. Results

3.1. Macroscopic characterization

A defect-free Cu—Al alloy/HSLA steel FGM part with no cracks or pores was obtained. Fig. 3(a) depicts the macrograph of the cross-section of the FGM part. Fig. 3(b) depicts the region only composed by the Cu—Al alloy, in which a mixture of a predominant Cu (FCC) phase (white regions) with β phase at the intercellular regions (dark regions) can be noticed. The size of the Cu (FCC) constituents ranges from 15 to 110 μm. The micrograph of Fig. 3(c) is taken from an area with only HSLA steel and presents the characteristic ferrite grain boundaries with a grain size ranging from 1 to 4 μm as also previously observed in Duarte et al.[15]. Scanning Electron Microscope images of the microstructure at the interface region are detailed in Fig. 3(d), (e), (f) and (g). In region D, both β phase and small Fe (BCC) constituents in a Cu (FCC) matrix were observed. In regions E, F, and G (higher Fe content regions) it can be perceived the existence of both Fe (BCC) (grey features) with Cu (FCC) (light features) at the intercellular regions. Since both wires were not deposited at the same time, this mixture arises from intense convective motion in the molten pool created by the Lorentz force, Buoyancy Force, Surface Tension gradient, and arc shear stress [16]. When moving upwards from region G to D a reduction in the Fe (BCC) constituents can be perceived, as we moved closer to the region unaffected by the steel elements (region D). The morphologies of the Fe constituents in regions D and E are of a dendritic type, and a globular type in regions F and G.

3.2. Synchrotron radiation measurements

Fig. 4 details the synchrotron X-ray diffraction patterns taken from the cross-section of the FGM part. The diffraction patterns reveal that the HSLA steel region is composed of Fe (BCC) and Fe (FCC) constituents, corresponding to ferrite and austenite, respectively. In the Cu—Al alloy region, a mixture of several crystalline phases including Cu (FCC), $AlCu_3$ ($D0_{19}$), Al_4Cu_9 (γ_1), $AlCu_3$ (β) are observed. At the joining interface, no intermetallics were found. The main phases of each alloy were observed in the diffraction patterns obtained from the interfacial region: Fe (BCC), and Fe (FCC), together with Cu (FCC). This result is in good agreement with the interface micrographs previously depicted in Fig. 3(d), (e), (f) and (g), where no other intermetallics were discernible at this location. This result indicates that these two alloys used can be used together with GTAW-WAAM, without the appearance of potentially undesirable phases in the bonding area.

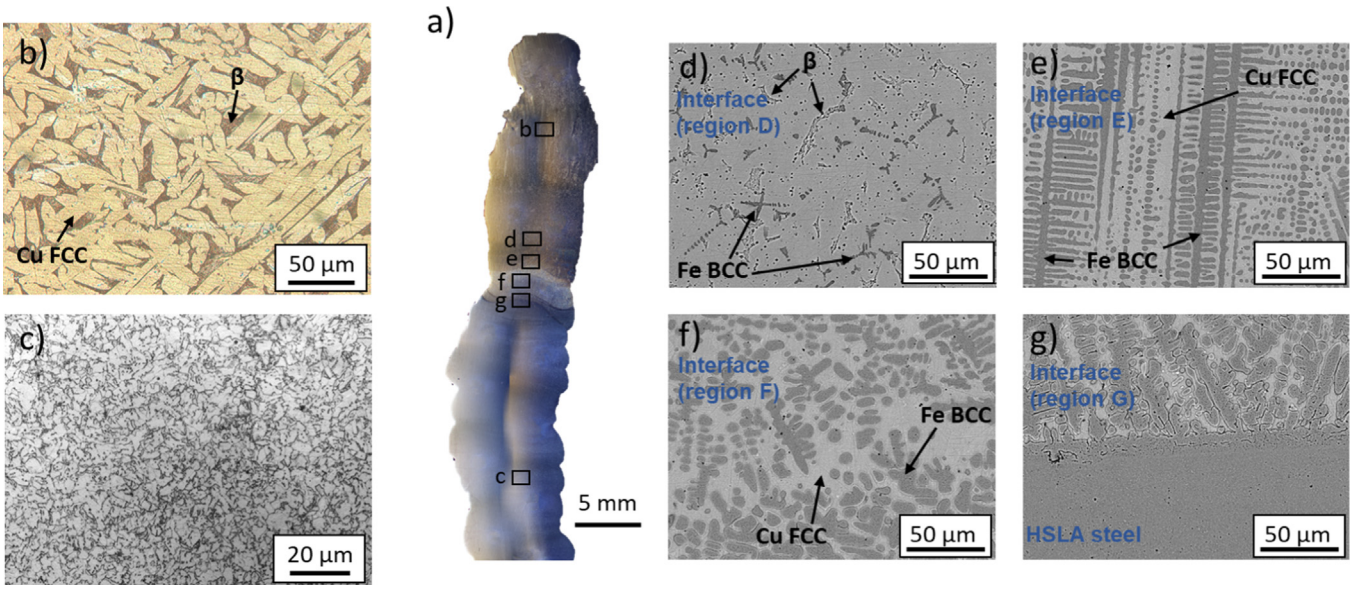

Fig. 3. (a) Cross-section overview of the as-built FGM part; Detail of the region with: (b) 100% HSLA steel, (c) 100% Cu—Al alloy, (d), (e), (f) and (g) interfacial regions.

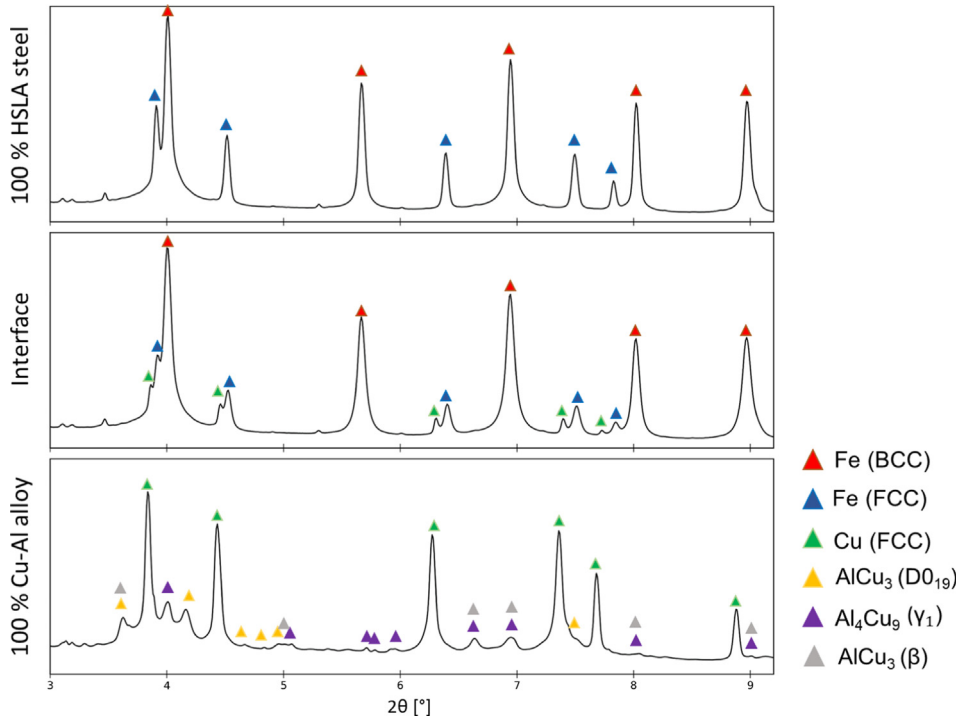

Fig. 4. Synchrotron X-ray diffraction analysis performed in regions comprising only HSLA steel, Cu—Al alloy, and in the interface (region e, previously depicted in Fig. 3).

3.3. Scanning electron microscopy analysis

The results of the elemental mapping compositions measured by SEM-EDS in the region of HSLA steel, Cu—Al alloy, and at the interface are given in Fig. 5, Fig. 6, and Fig. 7, respectively. The content in the steel region is mainly composed of Fe, but Mo and Ni were also measured (refer to Fig. 5b,c). The EBSD map (Fig. 5d) along the build-up direction revealed a near-equiaxed microstructure at the HSLA region of the FGM, unlike the typical columnar grains that are found during WAAM of other engineering alloys [17]. Moreover, these equiaxed grains did not reveal any preferential orientation (Fig. 5d). Such equiaxed grains are commonly seen in WAAM of HSLA steel [18] and are a consequence of the solid solution transformations of Fe (FCC) to Fe (BCC).

EDS measurements made in the Cu—Al base material (Fig. 6) revealed compositional changes between the β-phase and the remaining Cu (FCC) matrix. Besides Cu and Al, the Cu—Al wire also has a considerable amount of Fe present (0.8 wt%) in its composition, therefore the quantity of these three elements was evaluated. A reduction in the amount of Cu along the grain boundaries (Fig. 6a) was found, contrasting with the larger amount of Fe which migrated to these regions during solidification (Fig. 6c).

Al was found in higher amounts within the β regions (Fig. 6b) and depleted at the Cu (FCC) regions. This is a consequence of the precipitation of Al-rich (Al_4Cu_9) in the β ($AlCu_3$) regions, which are Al-rich regions. At higher magnification, it is possible to observe the existence of different precipitates inside the β regions (Fig. 6d). The EDS scan line across the β regions (Fig. 6e) showed a

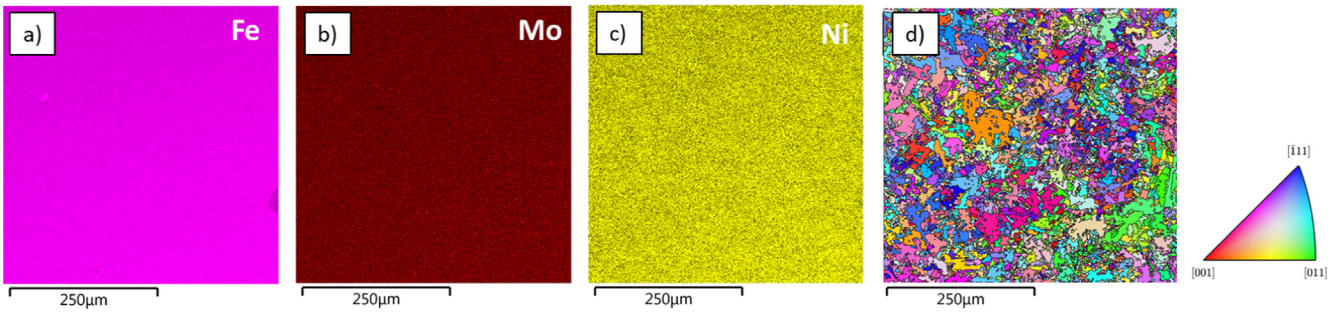

Fig. 5. Energy-dispersive X-ray spectroscopy (EDS) mapping of the as-built HSLA steel region: (a) Fe; (b) Mo, (c) Ni, (d) Electron Backscatter Diffraction (EBSD) inverse pole figure.

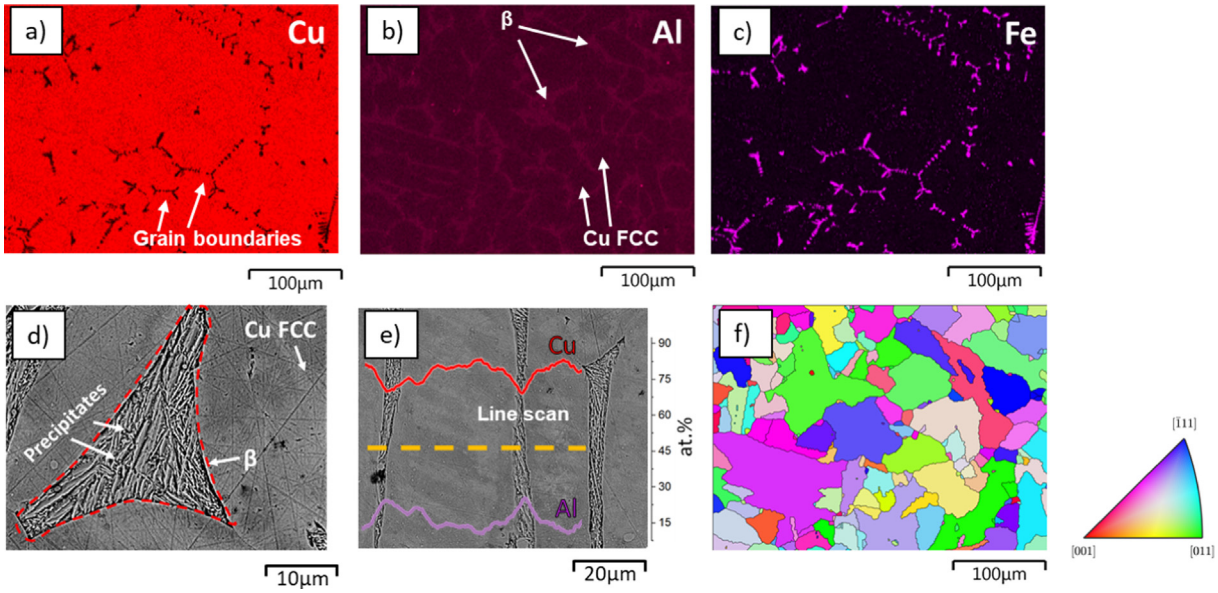

Fig. 6. Elemental mapping of the as-built copper microstructures obtained by scanning electron microscopy coupled with energy dispersive X-ray spectrometry (SEM-EDS): (a) Cu, (b) Al, (c) Fe; (d) Scanning electron microscopy (SEM) image of the secondary phases and precipitates found in the as-built copper alloy; (e) EDS line scan across Cu-based alloy secondary phases; (f) EBSD orientation maps.

decrease in the Cu content and an increase in the Al, as the stoichiometry of these regions follows the composition of the constituents identified by X-ray diffraction (Al_4Cu_9). EBSD mapping of the Cu-alloy (Fig. 6f) shows equiaxed grains, without any preferential orientation.

Although SEM-EDS is a semi-quantitative analysis technique, it still enables to evaluate the tendency of the element's distribution along the interface region of the FGM part. Fig. 7 presents two EDS maps taken at the interfacial area. Fig. 7(a), (b) and (c) depicts the first EDS map scan made between the interface region G and the HSLA-steel. No Cu and Al were found in the HSLA-steel section, but both are present in region G, previously identified by a mixture of Fe (BCC) with Cu (FCC) at the intercellular regions (Fig. 3g). In contrast, the amount of Fe decreases in the interfacial area, when Cu and Al start to blend in with the steel. In the second EDS map scan (Fig. 7(d), (e) and (f)), taken from the interface between regions E and F (refer to Fig. 3e,f), an inverse relationship between the amount of Fe and Cu can be perceived, i.e., with the increase in the amount of Cu (as we move closer to the region of 100% Cu—Al alloy), the amount of Fe decreases.

Fig. 8(a) depicts an EBSD phase map taken at the FGM interface. The region of HSLA steel is mainly composed of small equiaxed grains of BCC-type (Ferrite), while the interface shows a columnar-dendritic microstructure, highly oriented perpendicularly to the fusion line. Moreover, the coarse elongated grains are of BCC-type, indicating an incomplete transformation of δ-ferrite to γ. Higher magnification SEM images in the interface region (Fig. 8b,c) revealed that the Fe (BCC) constituents in the HSLA steel and the interface regions have different morphologies. In the region of the HSLA steel, it was observed the presence of MA (Martensite-Austenite) constituents and α-ferrite. The presence of MA constituents in low-alloyed steel is attributed to an incomplete transformation of austenite to martensite during multiple reheatings to critical temperatures [19]. In the interface region, the elongated Fe-dendrites are δ-ferrite. EDS point analysis (Fig. 8d) was conducted to determine the chemical composition of the Fe and Cu constituents in the interface region. It was determined that δ-ferrite contains up to 11% of Cu, and the Cu (FCC) constituents hold up to 5% of Fe. This change in the composition of the Fe constituents might be responsible to hinder the complete transformation of δ-ferrite during solidification.

3.4. Hardness, electrical conductivity, and electrical impedance measurements

Fig. 9 depicts the hardness measurements along the height of the Cu—Al/HSLA-steel part. A good agreement exists between the macrograph presented in Fig. 3(a) and the hardness measurements.

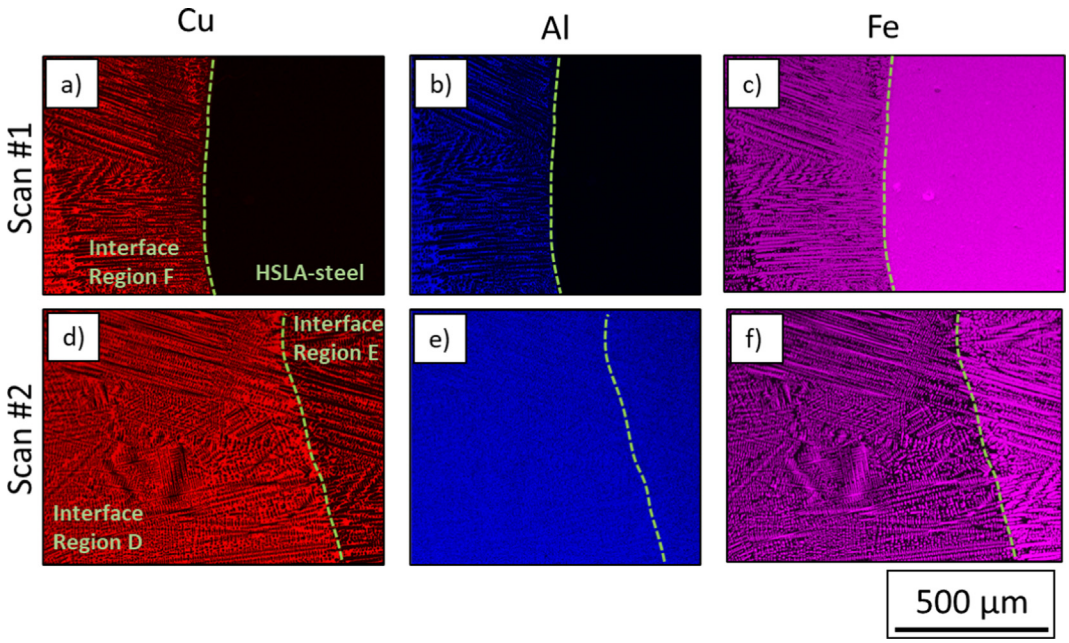

Fig. 7. EDS mapping of the HSLA-steel to Cu—Al interface region analysis: Scan #1: (a) Cu, (b) Al, (c) Fe; Scan #2: (d) Cu, (e) Al, (f) Fe.

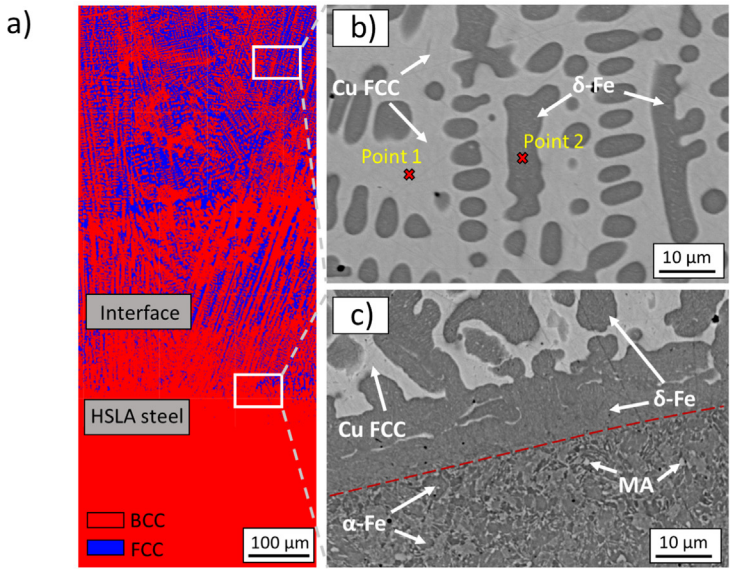

d)

(wt. %)

	Point 1	Point 2
Fe	4.89	85.22
Cu	90.27	10.96
Al	4.84	3.82

Fig. 8. (a) EBSD phase mapping of the interface region; (b) SEM morphologies of δ-ferrite in a Cu FCC matrix; (c) SEM morphologies of MA constituents in an α-Fe matrix; (d) EDS point analysis at positions marked in (b). MA: Martensite-austenite.

In particular, the region identified as being only composed of HSLA-steel (height < 15 mm) has an average hardness of 250 HV. This value is closely related to its microstructure (polygonal ferrite + MA); a similar value was also observed in the as-built WAAM and weld metal [20]. As we move closer to the interface region, the hardness decreases to 197 HV, approximately. This was attributed to an increase of the Cu content and an increase of the α-Fe (BCC) grain size near the interface. The Cu-alloy layers were deposited with higher energy than the steel layers, which reduced the cooling rate and promoted for larger polygonal α-ferrite to form and grow. In region G, the hardness drops to around 180 HV, this result is associated with the change of HSLA steel constituents from polygonal α-ferrite + MA islands to a majority of coarse dendritic δ-ferrite. The slight hardness increase to 200 HV in regions F and E was attributed to the dual-phase microstructure (δ-Ferrite + Cu (FCC) constituents) and its multiple iterations, similar to what occurs in duplex stainless steels [20–22]. Towards the end of the interface, a smooth transition of hardness exists due to the continuous decrease in Fe (BCC constituents). This gradual hardness transition is in good agreement with the SEM images previously depicted in Fig. 3(d), (e), (f), and (g), which did not show high hardness constituents (e.g., martensite), characteristic of dissimilar welding [23–25]. In addition, it was also observed a gradual variation in the number and size of Fe (BCC) constituents along the interface region.

The electrical conductivity and electrical impedance measurements are presented in Fig. 10. In the steel region, the electrical conductivity is on average of 5.2% IACS and increases to 11.1% IACS in the region that is only composed by the Cu—Al alloy. Both techniques used to characterize electrical properties are very sensitive

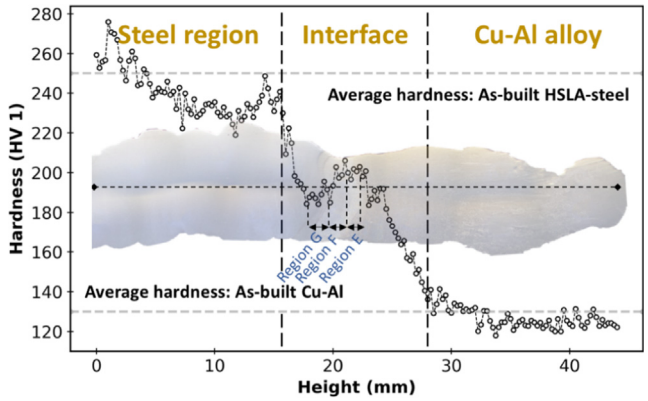

Fig. 9. Hardness measurements taken from the substrate to the last deposited layer of the FGM cross-section.

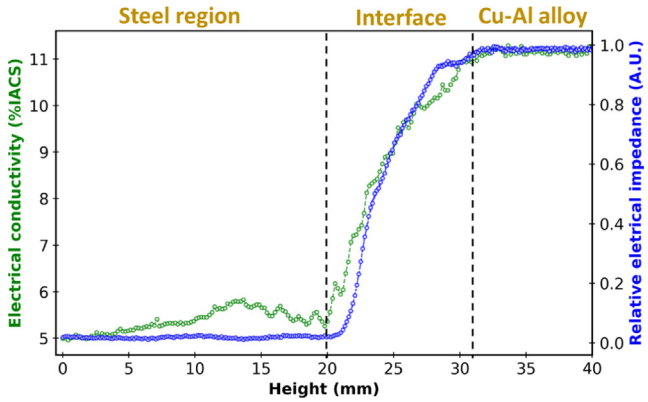

Fig. 10. Electric conductivity and electrical impedance measurements taken from the first to the last deposited layer of the FGM cross-section.

to the amount of each alloy, which allows quantifying the extension of the interfacial region. With these techniques and with the hardness measurements a length of 12 mm was measured for the interface region. This large interface region is due to the diffusion of elements between both materials that occurs during the deposition of subsequent layers and is not confined between the last steel and first Cu—Al alloy deposited layers.

3.5. Uniaxial tensile testing

Representative stress–strain curves of both single HSLA steel, Cu—Al, and FGM samples are detailed in Fig. 11. It can be observed that the ultimate tensile strength of the HSLA-steel is significantly higher than the Cu—Al alloy base material (753 vs 502 MPa). The elongation to fracture between the base materials is higher in the Cu—Al alloy (35.2 vs 24.6%). As for the FGM part, it can be observed that the tensile strength is between that of the two base materials (690 MPa), while the fracture strain is lower than both base materials (16.6%). The fracture surface of the functionality graded material indicates a mixture of a ductile-like fracture, with the presence of dimples, and a quasi-cleavage type fracture, with the presence of cleavage facets (Fig. 11b). The fracture surface of the control HSLA steel sample is mainly composed of dimples, indicating a ductile-like type fracture (Fig. 11c). In all tested samples taken from the FGM part, the fracture appeared in the Cu—Al side near the interface (Fig. 11d). As for the as-built Cu-alloy, SEM images show a predominant existence of dimples with small regions of cleavage facets, which indicates that the fracture is predominantly dominated by a ductile fracture.

4. Discussion

Based on the Cu—Fe phase diagram (Fig. 12a), joining Cu to steel is challenging. The Fe—Cu system possesses a nearly flat liquidus line, and, therefore, a submerged miscibility gap exists that can be accessed by undercooling the melt. Cu—Fe is characterized by a large enthalpy of mixing, i.e., if the melt in the interface area cools rapidly, the weld pool will undercool, causing a separation of the liquid phase into a Fe-rich melt (L1) and Cu-rich melt (L2). Thus, leading to solidification below the liquid metastable miscibility gap. In the binary Cu—Fe phase diagram the position of this miscibility gap is right below the liquidus line, consequently, small undercooling is sufficient to promote this separation of liquid phases [26]. After the liquid-phase separation, both liquid phases are in an undercooled state, thus, the L1 (Fe-rich) phase solidifies as the leading phase, since it will be the phase possessing a higher undercooling, which will be the preferential nucleation site [5]. Based on the Cu—Al binary phase diagram (Fig. 12b) it can be perceived that the depletion of Al content in the Cu FCC constituents located at the interface region (refer to Fig. 8), from 8.5 wt% in the Cu—Al alloy down to 4.8 wt%, resulted in a change in the alloy composition which prevents the solidification reaction liquid → β, leading to the absence of solid-state transformations. This corroborates with the non-existence of β and other phases in the regions E, F, and G since the liquid directly transforms to Cu-FCC.

In the SEM images (Fig. 3d, e, f, g) the Cu and Fe solute distributions at the interface are visible, without the formation of Fe-rich or Cu-rich spheres morphology that would form if the material entered the metastable miscibility gap [29]. The existence of highly aligned Fe columnar dendrites (EBSD, Fig. 8a) also suggests that the melt at the interface did not experience sufficient undercooling to enter the metastable liquid miscibility gap, resulting from the normal liquid–solid phase transformation [30]. Due to a low ΔT before nucleation, the δ-ferrite (Fe-BCC) in the interface region is the first to solidify without entering the metastable miscibility gap. Then, the Cu-rich region (FCC) will originate due to the continuous solute segregation to the remaining liquidus during solidification [27]. Following, around 800–900 °C, the Fe (BCC) will experience transformation into Fe (FCC). Similar behavior has been found in the literature, where the mixture of a Fe with a Cu alloy did not result in entering the miscibility gap [27,29]. Fig. 13 details a thermodynamic calculation that considers a conservative dissolution of only 30% of the Cu—Al alloy in the HSLA steel. In the equilibrium phase diagram, it can be noticed that δ-ferrite does not completely transform during cooling. In addition, due to the higher cooling rate of WAAM, the δ-ferrite to austenite transformation is suppressed [31]. These results alongside the EBSD data (Fig. 8a), with highly oriented columnar dendrites in the interface, corroborate the thesis that the increase of the Cu—Al content stabilized the δ-ferrite in the transition zone.

From the synchrotron X-ray diffraction measurements, different phases were revealed in the Cu—Al alloy: Cu (FCC), $AlCu_3$ ($D0_{19}$), Al_4Cu_9 (γ_1), $AlCu_3$ (β). These results are in good agreement with the SEM image of the Cu—Al base material (Fig. 6) since Al was found in higher quantity within the β ($AlCu_3$) regions. When the X-ray beam was focused on the interface area, the intermetallics of the Cu—Al base material ($AlCu_3$ ($D0_{19}$), Al_4Cu_9 (γ_1), $AlCu_3$ (β)) were *not* found, neither Cu—Al-Fe nor Fe-Al intermetallics, as found in others studies [32–34]. Nevertheless, in region D, far from the last deposited steel layers, both $AlCu_3$ (β)) and Fe (BCC) phases were found, but both in small quantities.

Tensile test specimens' fracture in the Cu side near the interface region with two distinct fracture modes: ductile-like and a quasi-cleavage fracture. The fact that the FGM part had less elongation to fracture than both base materials indicates that these have a lar-

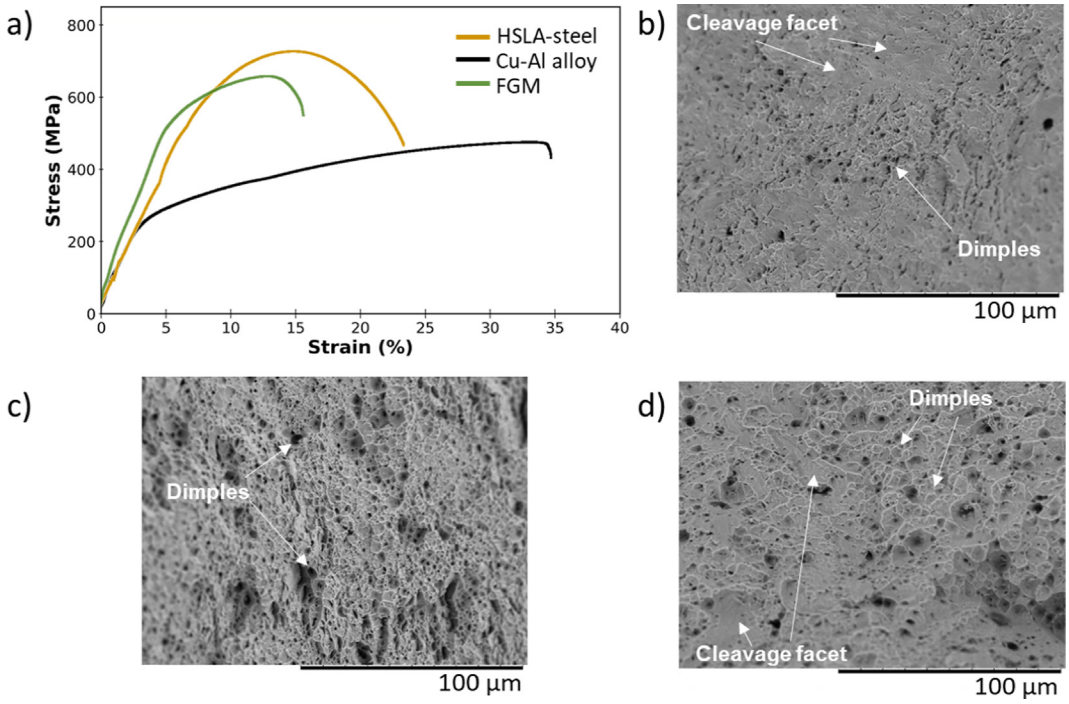

Fig. 11. (a) Representative stress–strain curves of the HSLA-steel and Cu—Al alloy parts and their dissimilar multi-metallic part; SEM image of the fracture surface of (b) Functionality graded material; (c) As-built HSLA steel; (d) As-built Cu—Al alloy.

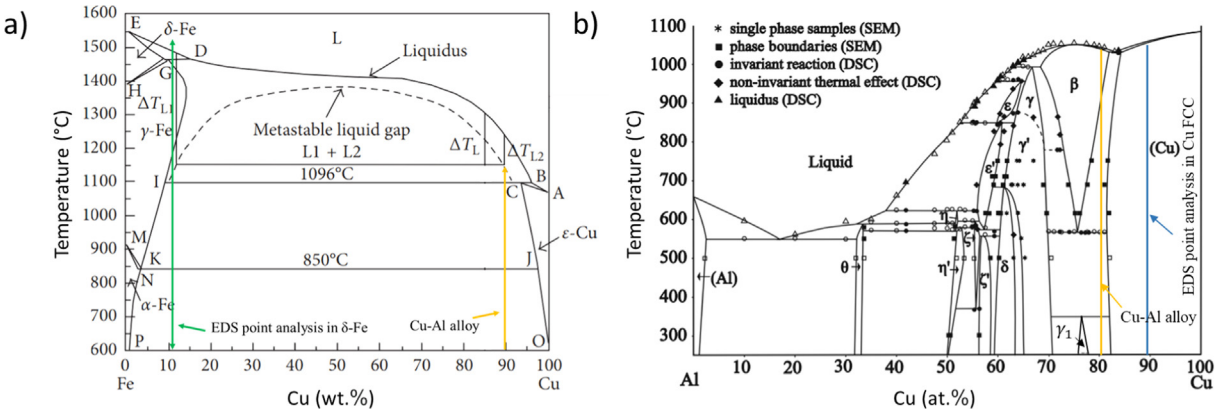

Fig. 12. (a) Cu—Fe Phase diagram with the metastable miscibility gap (dotted curved line) (adapted from [27]), pointing to the composition of the δ-Fe constituent; (b) Cu—Al binary phase diagram highlighting the composition in the Cu-FCC constituents in the interface (adapted from [28]).

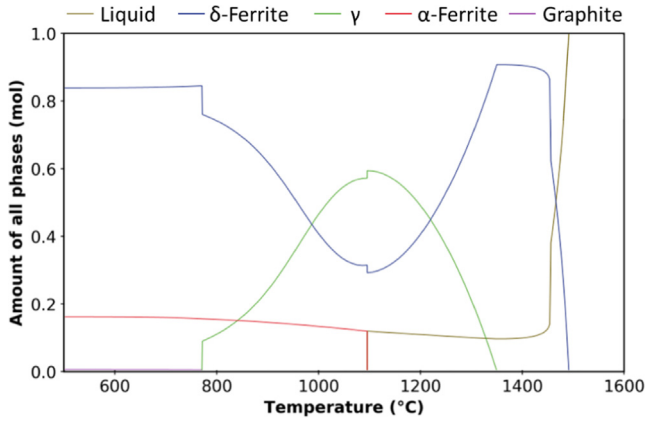

Fig. 13. Calculated equilibrium phase diagram considering an alloy with 70% of the HSLA steel and 30% of the Cu—Al alloy elements (wt.%) in the molten pool.

ger deformation ability than the material near the interface which is unable to maintain high strain. The reason for such behavior is related to the microstructure in this region (Fig. 3d and e), which involves a combination of a dendritic-type structure of Fe phases and β precipitates in a Cu matrix. The incoherent microstructures can create several potential crack nucleation and propagation points, decreasing the ductility near the interface. Despite this, the absence of hardness peak in the interface region allowed a considerable ductility (16.6%). The increase in the tensile strength in comparison with the Cu—Al base material is attributed to the Fe-constituents mixed in the Cu matrix. During the tensile testing, the stresses will be first accommodated by the softest material (Cu—Al), then the stress will be transferred to a harder and brittle region, and from that point on, deformation will no longer be possible, resulting in the fracture surface as depicted in Fig. 11(b). These results confirmed that with T-WAAM an effective soft transition from HSLA-steel to Cu—Al alloy is possible, without the existence of defects, and with excellent strength and ductility.

5. Conclusions

This work investigated the fabrication of an HSLA-steel to copper–aluminum alloy functionally graded material using the twin-wire and arc additive manufacturing (T-WAAM) technique. The FGM revealed no defects and had excellent high strength and ductility in the interface. The major conclusions can be drawn:

- A mixture of Cu (FCC) and Fe (BCC) phases was visible in the interface region by scanning electron microscopic analysis. These Fe (BCC) phases were found to be residual δ-ferrite by EDS measurements, thermodynamic calculations, and EBSD.
- Synchrotron X-ray diffraction measurements showed no brittle intermetallic phases at the interfacial region.
- At the interface region, a gradient of composition, hardness, electrical conductivity, and electrical impedance was obtained. Even though an abrupt transition was made with these two materials, the consequent remelting, and heating of previously deposited layers, when a new one is added, resulted in a large interface region (≈12 mm). This fact demonstrates the potential of WAAM to be used for FGM's fabrication.
- A tensile strength of 690 MPa and an elongation at fracture of 16.6% were achieved in the FGM part, thus allowing the use of such components in structural applications. The fracture occurred in the Cu region near the interface, in which the microstructure involves a combination of a dendritic-type structure of Fe (BCC) phases and β precipitates in a Cu matrix, demonstrating that the interface strength is higher than the copper-only region.

CRediT authorship contribution statement

Tiago A. Rodrigues: Investigation, Validation, Data curation, Writing – original draft. **N. Bairrão:** Investigation, Validation. **Francisco Werley Cipriano Farias:** Software, Investigation, Writing – original draft. **A. Shamsolhodaei:** Investigation, Resources. **Jiajia Shen:** Investigation, Software. **N. Zhou:** Resources. **Emad Maawad:** Resources, Data curation. **Norbert Schell:** Resources, Writing – review & editing. **Telmo G. Santos:** Conceptualization, Supervision, Project administration, Funding acquisition. **J.P. Oliveira:** Supervision, Writing – review & editing, Funding acquisition.

Declaration of Competing Interest

The authors declare that they have no known competing financial interests or personal relationships that could have appeared to influence the work reported in this paper.

Acknowledgments

TAR acknowledges FCT – MCTES for funding the Ph.D. grant SFRH/BD/144202/2019. TAR, JS, TGS, and JPO acknowledge Fundação para a Ciência e a Tecnologia (FCT – MCTES) for its financial support via the project UID/00667/2020 (UNIDEMI). This activity has received funding from the European Institute of Innovation and Technology (EIT) – Project Smart WAAM: Microstructural Engineering and Integrated Non-Destructive Testing. This body of the European Union receives support from the European Union's Horizon 2020 research and innovation programme.

References

[1] T.A. Rodrigues, V. Duarte, R.M. Miranda, T.G. Santos, J.P. Oliveira, Current status and perspectives on wire and arc additive manufacturing (WAAM), Materials (Basel) 12 (7) (2019) 1121, https://doi.org/10.3390/ma12071121.
[2] C. Zhang, F. Chen, Z. Huang, M. Jia, G. Chen, Y. Ye, Y. Lin, W. Liu, B. Chen, Q. Shen, L. Zhang, E.J. Lavernia, Additive manufacturing of functionally graded materials: a review, Mater. Sci. Eng., A 764 (2019) 138209, https://doi.org/10.1016/j.msea.2019.138209.
[3] C. Tan, Y. Chew, G. Bi, D. Wang, W. Ma, Y. Yang, K. Zhou, Additive manufacturing of steel–copper functionally graded material with ultrahigh bonding strength, J. Mater. Sci. Technol. 72 (2021) 217–222, https://doi.org/10.1016/j.jmst.2020.07.044.
[4] T.A. Mai, A.C. Spowage, Characterisation of dissimilar joints in laser welding of steel – kovar , copper – steel and copper – aluminium, 2019. https://doi.org/10.1016/j.msea.2004.02.025.
[5] X. Sun, W. Hao, G. Geng, T. Ma, Y. Li, Solidification microstructure evolution of undercooled Cu-15 wt.% Fe alloy melt, Adv. Mater. Sci. Eng. 2018 (2018), https://doi.org/10.1155/2018/6304518.
[6] S. Chen, J. Huang, J. Xia, H. Zhang, X. Zhao, Microstructural characteristics of a stainless steel/copper dissimilar joint made by laser welding, Metall. Mater. Trans. A Phys. Metall. Mater. Sci. 44 (8) (2013) 3690–3696, https://doi.org/10.1007/s11661-013-1693-z.
[7] S. Chen, J. Huang, J. Xia, X. Zhao, S. Lin, Influence of processing parameters on the characteristics of stainless steel/copper laser welding, J. Mater. Process. Technol. 222 (2015) 43–51, https://doi.org/10.1016/j.jmatprotec.2015.03.003.
[8] M. Velu, S. Bhat, Metallurgical and mechanical examinations of steel-copper joints arc welded using bronze and nickel-base superalloy filler materials, Mater. Des. 47 (2013) 793–809, https://doi.org/10.1016/j.matdes.2012.12.073.
[9] X. Zhang, C. Sun, T. Pan, A. Flood, Y. Zhang, L. Li, F. Liou, Additive manufacturing of copper – H13 tool steel bi-metallic structures via Ni-based multi-interlayer, Addit. Manuf. 36 (2020) 101474, https://doi.org/10.1016/j.addma.2020.101474.
[10] U. Articek, M. Milfelner, I. Anzel, Synthesis of functionally graded material H13/Cu by LENS technology, Adv. Prod. Eng. Manag. 8 (3) (2013) 169–176, https://doi.org/10.14743/apem2013.3.164.
[11] X. Shu, G. Chen, J. Liu, B. Zhang, J. Feng, Microstructure evolution of copper/steel gradient deposition prepared using electron beam freeform fabrication, Mater. Lett. 213 (2018) 374–377, https://doi.org/10.1016/j.matlet.2017.11.016.
[12] K. Wang, S.-L. Shang, Y. Wang, A. Vivek, G. Daehn, Z.-K. Liu, J. Li, Unveiling non-equilibrium metallurgical phases in dissimilar Al-Cu joints processed by vaporizing foil actuator welding, Mater. Des. 186 (2020) 108306, https://doi.org/10.1016/j.matdes.2019.108306.
[13] T.G. Santos, R.M. Miranda, P. Vilaça, J.P. Teixeira, J. dos Santos, Microstructural mapping of friction stir welded AA 7075–T6 and AlMgSc alloys using electrical conductivity, Sci. Technol. Weld. Join. 16 (7) (2011) 630–635, https://doi.org/10.1179/1362171811Y.0000000052.
[14] G.L. Sorger, J.P. Oliveira, P.L. Inácio, N. Enzinger, P. Vilaça, R.M. Miranda, T.G. Santos, Non-destructive microstructural analysis by electrical conductivity: comparison with hardness measurements in different materials, J. Mater. Sci. Technol. 35 (3) (2019) 360–368, https://doi.org/10.1016/j.jmst.2018.09.047.
[15] V.R. Duarte, T.A. Rodrigues, N. Schell, T.G. Santos, J.P. Oliveira, R.M. Miranda, Wire and arc additive manufacturing of high-strength low-alloy steel: microstructure and mechanical properties, Adv. Eng. Mater. (2021), https://doi.org/10.1002/adem.202001036.
[16] S. Kou, Welding Metallurgy, John Wiley and Sons, 1987. https://doi.org/10.1002/0471434027.
[17] Y. Yehorov, L.J. da Silva, A. Scotti, Exploring the use of switchback for mitigating homoepitaxial unidirectional grain growth and porosity in WAAM of aluminium alloys, Int. J. Adv. Manuf. Technol. 104 (1-4) (2019) 1581–1592, https://doi.org/10.1007/s00170-019-03959-w.
[18] T.A. Rodrigues, V. Duarte, J.A. Avila, T.G. Santos, R.M. Miranda, J.P. Oliveira, Wire and arc additive manufacturing of HSLA steel: effect of thermal cycles on microstructure and mechanical properties, Addit. Manuf. 27 (2019), https://doi.org/10.1016/j.addma.2019.03.029.
[19] A. Lambert-Perlade, A.F. Gourgues, J. Besson, T. Sturel, A. Pineau, Mechanisms and modeling of cleavage fracture in simulated heat-affected zone microstructures of a high-strength low alloy steel, Metall. Mater. Trans. A Phys. Metall. Mater. Sci. 35 (13) (2004) 1039–1053, https://doi.org/10.1007/s11661-004-1007-6.
[20] L. Han, T. Han, G. Chen, B. Wang, J. Sun, Y. Wang, Influence of heat input on microstructure, hardness and pitting corrosion of weld metal in duplex stainless steel welded by keyhole-TIG, Mater. Charact. 175 (2021) 111052, https://doi.org/10.1016/j.matchar.2021.111052.
[21] Y. Zhang, F. Cheng, S. Wu, The microstructure and mechanical properties of duplex stainless steel components fabricated via flux-cored wire arc-additive manufacturing, J. Manuf. Process. 69 (2021) 204–214, https://doi.org/10.1016/j.jmapro.2021.07.045.
[22] J. Verma, R.V. Taiwade, Dissimilar welding behavior of 22% Cr series stainless steel with 316L and its corrosion resistance in modified aggressive environment, J. Manuf. Process. 24 (2016) 1–10, https://doi.org/10.1016/j.jmapro.2016.07.001.
[23] B.T. Alexandrov, J.C. Lippold, J.W. Sowards, A.T. Hope, D.R. Saltzmann, Fusion boundary microstructure evolution associated with embrittlement of Ni-base alloy overlays applied to carbon steel, Weld. World. 57 (1) (2013) 39–53, https://doi.org/10.1007/s40194-012-0007-1.
[24] T. Soysal, S. Kou, D. Tat, T. Pasang, Macrosegregation in dissimilar-metal fusion welding, Acta Mater. 110 (2016) 149–160, https://doi.org/10.1016/j.actamat.2016.03.004.
[25] M. Rozmus-Górnikowska, Cieniek, M. Blicharski, J. Kusiński, Microstructure and microsegregation of an inconel 625 weld overlay produced on steel pipes

by the cold metal transfer technique, Arch. Metall. Mater. 59 (2014) 1081–1084, https://doi.org/10.2478/amm-2014-0185.
[26] M.A. Turchanin, P.G. Agraval, I.V. Nikolaenko, Thermodynamics of alloys and phase equilibria in the copper-iron system, J. Phase Equilibria. 24 (4) (2003) 307–319, https://doi.org/10.1361/105497103770330280.
[27] Y.Z. Chen, F. Liu, G.C. Yang, X.Q. Xu, Y.H. Zhou, Rapid solidification of bulk undercooled hypoperitectic Fe-Cu alloy, J. Alloys Compd. 427 (1-2) (2007) L1–L5, https://doi.org/10.1016/j.jallcom.2006.03.012.
[28] O. Zobac, A. Kroupa, A. Zemanova, K.W. Richter, Experimental description of the Al-Cu binary phase diagram, Metall. Mater. Trans. A Phys. Metall. Mater. Sci. 50 (8) (2019) 3805–3815, https://doi.org/10.1007/s11661-019-05286-x.
[29] A. Zafari, K. Xia, Laser powder bed fusion of ultrahigh strength Fe-Cu alloys using elemental powders, Addit. Manuf. 47 (2021) 102270, https://doi.org/10.1016/j.addma.2021.102270.
[30] S. Liu, J. Jie, Z. Guo, G. Yin, T. Wang, T. Li, Solidification microstructure evolution and its corresponding mechanism of metastable immiscible Cu80Fe20 alloy with different cooling conditions, J. Alloys Compd. 742 (2018) 99–106, https://doi.org/10.1016/j.jallcom.2018.01.306.
[31] L. Liao, S. Chumbley, Influence of cooling rate on the ferrite prediction diagram of duplex stainless steel castings, Metall. Mater. Trans. A Phys. Metall. Mater. Sci. 50 (5) (2019) 2435–2442, https://doi.org/10.1007/s11661-019-05166-4.
[32] S. Curiotto, R. Greco, N.H. Pryds, E. Johnson, L. Battezzati, The liquid metastable miscibility gap in Cu-based systems, Fluid Phase Equilibria 256 (1-2) (2007) 132–136, https://doi.org/10.1016/j.fluid.2006.10.003.
[33] L. Zhu, S. Soto-Medina, W. Cuadrado-Castillo, R.G. Hennig, M.V. Manuel, Materials & Design New experimental studies on the phase diagram of the Al-Cu-Fe quasicrystal-forming system, Mater. Des. 185 (2020) 108186, https://doi.org/10.1016/j.matdes.2019.108186.
[34] M. Gogebakan, B. Avar, Quasicrystalline phase formation in the conventionally solidified Al-Cu-Fe system Quasicrystalline phase formation in the conventionally solidified Al – Cu – Fe system, 2009.